ADVANCED ENERGY MATERIALS
www.advenergymat.de

Molecular Insights into the Interfacial Phenomena at the Li Metal | Polymer Solid-State Electrolyte in Anode-Free Configuration During Li Plating-Stripping via Advanced Operando ATR-FTIR Spectroscopy

*Jian-Fen Wang, Matthias Weiling, Felix Pfeiffer, Kun-Ling Liu, and Masoud Baghernejad**

Solid-state batteries are regarded as safe and high-energy-density candidates for next-generation energy storage. However, gaining a mechanistic understanding of the interfacial phenomena under real electrochemically working conditions remains a major challenge for cells containing solid-state electrolytes. This work presents an in-house built attenuated total reflection fourier-transform infrared (ATR-FTIR) spectroscopy cell equipped with an internal temperature-control unit. This cell is used for operando characterization of interfacial processes between plated Li and polymer during Li plating/stripping. As a proof of concept, a polymer electrolyte (cr-PEO_{10}LiTFSI) containing poly(ethylene oxide), Li bis-(trifluoromethanesulfonyl)imide and crosslink-initiator benzophenone (BP) is introduced on a copper mesh as current collector at 60 °C. The developed ATR-FTIR spectroscopy setup provides detailed insights into the electrolyte degradation and reveals the crystallinity transformation of PEO at the interface during plating. Moreover, for the first time, the degradation of BP is observed. This compound, often overlooked in electrolyte systems due to its low concentration, is found to play a significant role in the interfacial electrochemistry process. Overall, this study provides a comprehensive overview of the characterization on the PEO electrolyte-lithium metal interface and introduces a novel perspective on the reaction of BP as a crosslinking initiator in the solid-state batteries.

1. Introduction

With the latest developments, state-of-the-art lithium-ion batteries (LIBs) are rapidly approaching the limit of their theoretical energy density. To meet the increasing demand for higher power and energy density, extensive research has been conducted on various battery materials and configurations in recent years.[1,2] Among different next-generation cell chemistries, Li metal batteries (LMBs) are considered promising due to Li metal exceptionally high theoretical capacity (3860 mAh g^{-1}) and the lowest standard redox potential of all metallic anode materials (−3.04 V vs SHE).[3,4] Moreover, anode-free Li metal batteries (AFLMBs) are regarded as promising battery configurations due to their potential for achieving even higher energy densities, thanks to the reduced anode volume.[5] In addition, AFLMBs can lower both the cost and energy consumption associated with anode preparation.[6,7] However, AFLMBs suffer from low Coulombic efficiencies (CE), primarily due to the parasitic reactions associated with electrolyte degradation during electrodeposition ("plating") of Li. This degradation leads to the formation of an interphase at the Li metal|electrolyte boundary, resulting in the loss of active Li and increased interfacial impedance during the electrodissolution/-deposition (stripping/plating) processes.[8–11] Moreover, the accumulation of unconstrained plated Li can lead to the formation of dendrites, which pose significant safety risks, especially in the presence of state-of-the-art carbonate-based liquid electrolytes. These needle-like dendrites can cause short circuits, leading to thermal runaway and potential explosion of the cell.[12–14] As a result, great attention is being directed toward the use of solid-state electrolytes (SSEs). SSEs offer a promising prospect due to their increased mechanical and chemical stability against Li metal, and effectively enhance safety by suppressing dendrite growth.[13–15] Additionally, compared to liquid electrolytes, SSEs are leakproof and exhibit low volatility, reducing the risk of gas production and the leakage of toxic gases.[16] Given the energy density and safety feature, anode-free solid-state batteries (AFSSB) are considered the ultimate configuration, offering the highest energy density along with enhanced safety.[17]

Among SSEs, solid polymer electrolytes (SPEs) have generated notable attention due to their exceptional flexibility and

J.-F. Wang, M. Weiling, F. Pfeiffer, K.-L. Liu, M. Baghernejad
Helmholtz-Institute Münster
IMD-4
Forschungszentrum Jülich GmbH
Corrensstrasse 46, 48149 Münster, Germany
E-mail: b.masoud@fz-juelich.de

The ORCID identification number(s) for the author(s) of this article can be found under https://doi.org/10.1002/aenm.202404569

DOI: 10.1002/aenm.202404569

adaptability compared to inorganic solid electrolytes. These properties allow for better interfacial contact between the electrolyte and electrode, leading to lower internal resistance compared to inorganic solid electrolytes.[16,18] Since 1970s, various structural designs and modifications of the polyether-based SPEs, such as polyethylene oxide (PEO), have been extensively studied in LMBs.[19,20] PEO-based SPEs are particularly favored because of their simple structure and the strong donor character of the oxygen atoms in the ether chains, which effectively coordinate Li ions, making them an ideal benchmark candidate for fundamental studies of SPE-based LMBs.[21,22]

Li bis-(trifluoromethanesulfonyl)imide (LiTFSI) has become the most commonly used Li salt in PEO-based SPEs, owing to its excellent chemical, electrochemical, and thermal stability. The high degree of charge delocalization in LiTFSI facilitates ionic dissociation within the PEO matrix, enhancing ionic conductivity.[23] Furthermore, some efforts have been made to improve the relatively weak mechanical strength of SPEs compared to inorganic solid electrolytes (ISEs). These efforts include enhancing the mechanical strength of the polymer backbone through side-chain modifications and incorporating crosslinkers or crosslink-initiators, such as benzophenone (BP)-like compounds. The addition of BP and the process of UV irradiation in polymer electrolyte increase the amorphicity and therefore induce the formation of smaller crystal structures at elevated temperatures, such as 60 °C.[24] This change in crystallinity can enhance the flexibility and toughness of PEO. Therefore, the crosslinked electrolytes not only present higher mechanical strength but also reduce the crystallinity of the polymers to further enhance the ionic conductivity of the electrolytes.[20,24–29]

Despite SPEs offering greater chemical and electrochemical stability compared to liquid electrolytes, electrolyte degradation, and interfacial reactions remain prevalent and inevitable.[2,13] Due to the critical impact of these interfacial reactions on battery capacity retention and lifespan, the formation of the solid electrolyte interface (SEI) has been extensively studied in liquid electrolyte systems.[30–34] Hence, as SPEs gained more attention, researchers have increasingly focused on the interfacial reactions of SPEs and electrodes, because of their crucial role in the performance of SSBs.[12,32,35–37]

To achieve a deeper understanding of the interfacial phenomena in SSBs and address the challenges arising from interfacial reactions, an emphasis on interfacial investigation by developing advanced characterization methodologies is essential. Typically, these characterizations are conducted post-mortem, but this approach can introduce artificial contamination to the samples.[38–41] To avoid this, in situ/operando characterization is considered a more effective approach to investigate the evolving interphases in real-time without the risk of contamination.[42–46] Moreover, it allows for the observation and detection of interfacial species under real-working conditions, providing dynamic insights into reaction mechanisms that post-mortem analyses cannot capture. However, successful conducting of operando investigations requires the development of specially designed methodologies compatible with the representative analytical technique. In the case of AFSSBs, this need arises due to the highly reactive nature of plated Li metal, the opacity of battery materials, and the challenges of integrating the analytical instruments in use.[42–45,47–49]

Among the various in situ/operando techniques for investigating the Li metal|polymer interface, in-situ/operando infrared spectroscopy has generated great attention due to its relatively straightforward combination with electrochemical techniques and its ability for fast data acquisition for dynamic investigations.[49] Chusid et al. studied the interface chemistry between Li metal and polymeric electrolytes using in-situ FTIR spectroscopy. They developed a spectro-cell setup equipped with a heater, allowing to acquired spectra of poly[ethylene oxide-2-(2-methoxyethoxy)ethyl glycidyl ether] (P(EO/MEEGE)) at OCV and after Li plating at 50 °C.[50] He et al. employed near-field infrared nano-spectroscopy, aided by atomic force microscopy to characterize graphene|Li|PEO electrolyte interfaces. The spectra were collected in different states of the cell (before/after heating and before/after plating), revealing that nonuniform Li plating on the surface of graphene would lead to variations in the SEI layer chemical composition. Besides, the intrinsic heterogeneities of pristine SPE affect Li ion local transport, resulting in inhomogeneous Li deposition and SEI formation.[51] In another study, Yamada et al. used operando attenuated total reflection infrared (ATR-IR) spectroscopy to investigate the interface of PEO electrolyte with sputtered Cu electrode at room temperature. By employing cyclic voltammetry, they investigated the reduction steps from OCV to 0 V. They reported that LiTFSI is first reduced at 2.00 V forming an inorganic SEI, and the C—O bond of PEO broke at 1.90 V to form a C═C—containing species. Consisting of these decomposition products, the most resistive SEI-like layer was found to be formed at 0.80 V. However, the C═C species was further reduced to alkyl-related species below 0.80 V, which further reduced the interfacial resistance.[52]

These studies highlight the powerful applicability of Fourier Transform Infrared (FTIR) spectroscopy for in-situ/operando interphase characterization. Nevertheless, the integration of operando measurements to monitor during the Li plating/stripping processes under elevated temperatures has yet to be implemented, leaving the investigation of SPE batteries under real-working conditions unexplored.

In this study, we present a comprehensive investigation of a polymer electrolyte interface with Li metal using advanced operando Attenuated Total Reflection Fourier Transform Infrared (ATR-FTIR) spectroscopy through an in-house designed spectro-electrochemical cell. This cell, a prototype of which was successfully employed in liquid electrolyte system in a previous study of our group, includes a high-precision heating unit to maintain a constant cell temperature of 60 °C, ensuring comparability with prior electrochemical studies utilizing PEO electrolytes for the purpose of higher ion conductivity.[20,53–55] Li plating/stripping processes were conducted in an anode-free configuration on a copper mesh electrode, allowing for real-time detailed dynamic investigation of the interfacial reactions between Li metal and both crosslinked (cr-PEO_{10}LiTFSI) and non-crosslinked (PEO_{10}LiTFSI) PEO electrolytes. The investigation methodology of the PEO-based model system in this work provides unique molecular-level insights into the degradation mechanism of electrolyte components, including BP crosslink-initiators, PEO polymer, and TFSI-anion surface excess, all during Li plating/stripping. This experiment provides innovative perspectives on the interfacial reactions between solid polymer electrolytes and Li metal. It also offers a perspective on the

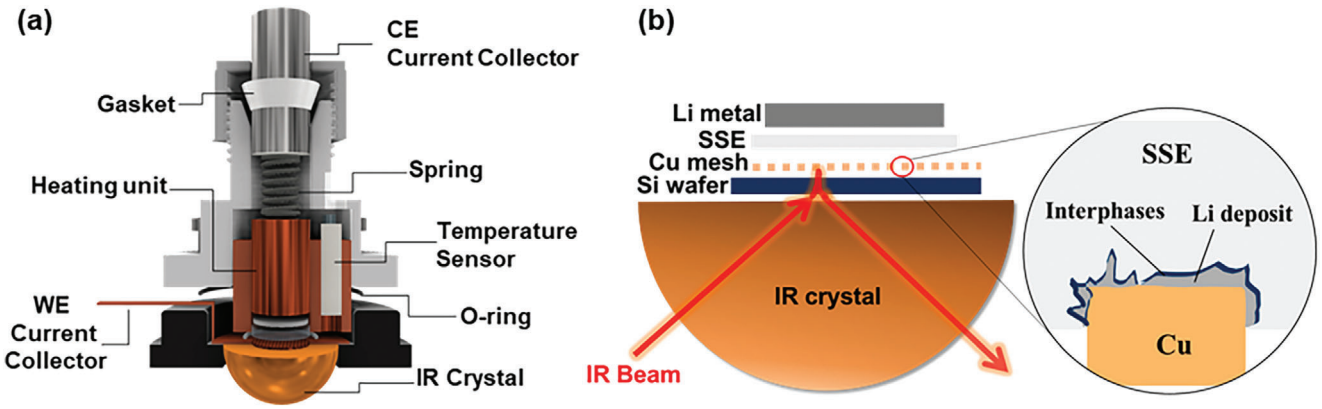

Figure 1. a) Schematic drawing of the spectro-electrochemical cell setup, with the integrated heating unit and the inner pressure regulating spring, enabling investigation under real-working conditions. b) Schematic drawing of the cell stack in the anode-free configuration.

application of a crosslink-initiator (BP) in polymer electrolyte, serving as a useful reference for future studies on the selection and utilization of materials for solid-state electrolytes.

2. Results and Discussion

2.1. Spectro-Electrochemical Cell Design and Configuration and Electrochemical Comparability of Copper Mesh as Current Collector

A scheme of our in-house 3D printed spectro-electrochemical cell, equipped with a high-precision internal heating unit is depicted in **Figure 1**a. Figure 1b illustrates the electrode configurations within the ATR-FTIR cell. In this configuration, an SSE, specifically a PEO-based polymer in this study, is brought into direct contact with the copper mesh, where Li plating/stripping occurs. Notably, a Si-wafer, chosen for its transparency of IR waves, is employed to protect the ATR crystal from reactions with Li species. Further details of the cell design can be found in the Experimental Section.

The use of copper mesh as a current collector instead of copper foil is necessary to ensure effective penetration of the IR beam, reaching the interface between plated Li and the polymer electrolyte. Although the surface area of this copper mesh differs by ≈80% from that of the copper foil, it is not the most conventional current collector for an anode-free configuration. Therefore, it is essential to evaluate its comparability with copper foil and optimize the current density accordingly.

To assess the feasibility of substituting copper foil with copper mesh as the current collector, the electrochemical performance of the cell with anode-free configuration using copper mesh is compared to that with copper foil in coin cell form. An electrochemical response of symmetric Li||Li coin cell was used as a benchmark for this comparison. **Figure 2** displays the corresponding voltage response in regard to the current densities of 0.01, 0.02, 0.05, 0.10, and 0.20 mA cm^{-2} for 2 h of both Li plating and stripping in the coin cells with the electrolyte consist of PEO polymer, LiTFSI salts, and BP (the crosslinked electrolyte, cr-PEO_{10}LiTFSI) at 60 °C.

The range of overvoltage values of the plating/striping is shown in Table S1 (Supporting Information). The Li|Li coin cell (blue diagram in Figure 2b), benefitting from the huge Li reservoir on both electrodes, exhibits a stable Li plating/stripping behavior with the lowest overvoltage compared to the cells with the anode-free configuration. Moreover, it scarcely shows a distinct voltage difference between plating and stripping overvoltage. The overvoltage values of the Li|Li cell increase linearly with the increased current density are depicted in Figure S1 (Supporting Information).

Nevertheless, coin cells with Li|Cu foil and Li|Cu mesh show notably higher overvoltage. Upon application of a 0.02 mA cm^{-2} current density, the Li|Cu mesh cell shows a plating plateau at −39.60 mV, and the Li|Cu foil cell shows a similar plating overvoltage plateau. However, they barely show a stripping plateau due to the short duration of the plating process. This indicates that only a small amount of Li metal was deposited with a small current density. In addition, most of the plated Li metal was consumed irreversibly. When applying a current of 0.05 mA cm^{-2} to the cells, a longer duration of the plating/stripping plateau is observed and the overvoltage plateaus of Li|Cu foil and Li|Cu mesh cells show a very slight difference. At this current density, the Li|Cu foil cell shows a higher plating overvoltage plateau at −83.40 mV compared to −60.20 mV of the Li|Cu mesh cell. Notably, when a current density of 0.10 mA cm^{-2} is applied, the plating overvoltage plateaus of both cells are prolonged. The Li|Cu mesh cell shows a plating plateau in the range from −82.90 to −227.60 mV, while the Li|Cu foil-based cell shows a relatively higher overvoltage plateau in the range from −117.10 to −302.20 mV. Although the duration of the plating/stripping plateaus is longer when applied 0.10 mA cm^{-2} to the cells, the distinct overvoltage difference between the Li|Cu mesh cell and the Li|Cu foil cell cannot be ignored. This becomes more evident when a current density of 0.20 mA cm^{-2} is applied, leading to severe polarization, increased overvoltage, and noise. These might stem from the different surface areas of copper foil and copper mesh. Therefore, the optimization of the current density is necessary when replacing copper foil with different types of current collectors.

The comparative results of the voltage profiles at various current densities indicate overvoltage differences between the use of the copper mesh and copper foil as a current collector. From these results, the current density of 0.05 mA cm^{-2} is

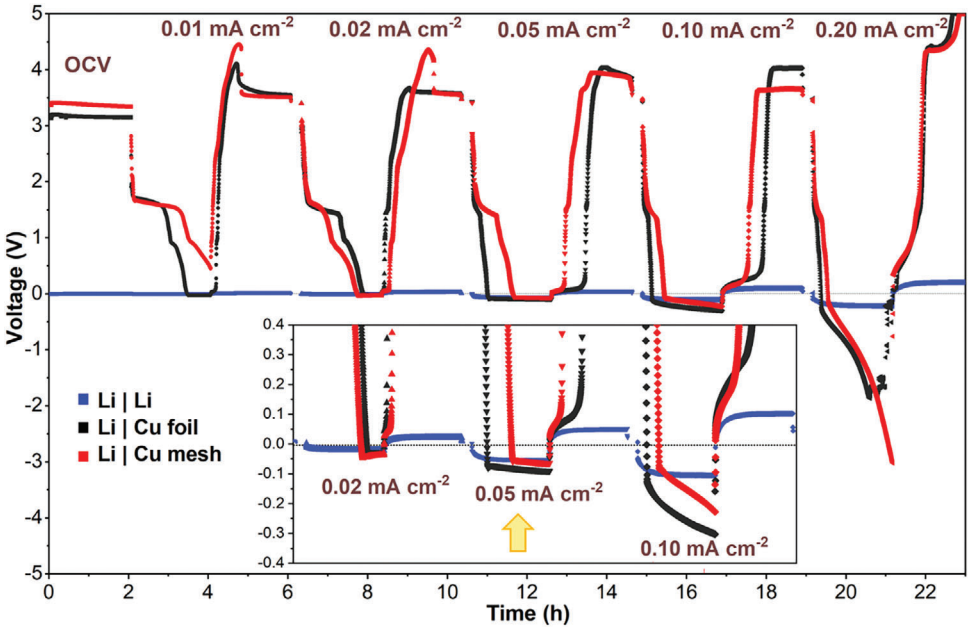

Figure 2. Voltage versus time profiles of copper foil and copper mesh current collector and Li metal applying $j = 0.01$, 0.02, 0.05, 0.10, and 0.20 mA cm^{-2} with cr-PEO$_{10}$LiTFSI as the electrolyte in the anode-free configuration coin cells at 60 °C.

identified as optimal for Li plating/stripping when using the copper mesh as a substitute for copper foil. At this current density, both Li|Cu foil and Li|Cu mesh cells exhibit similar plating overvoltage plateaus, and the copper mesh allows for sufficient plateau during plating, leading to a longer stripping plateau. Overall, these findings confirm the feasibility of using copper mesh as a current collector, and this configuration will be employed in further mechanistic investigation of the interfacial process during Li plating/stripping via ATR-FTIR spectroscopy.

2.2. ATR-FTIR Spectroscopy of Li Metal and PEO-Based Electrolyte

First, a systematic investigation of IR spectra and relevant band assignments for the different electrolyte components — PEO polymer, LiTFSI salt, and BP crosslink initiator — and their mixed composition was conducted to ensure accurate band assignment during operando measurements and serve as references. Detailed IR characteristics and corresponding assignments, supported by computational IR vibration modes, can be found in Tables S2–S5 (Supporting Information). Briefly, Figure S2 (Supporting Information) shows the full spectra and some extracted spectra areas with observable band changes of pure materials to combined materials. Notably, the band ≈1652 cm^{-1} of the cr-PEO$_{10}$LiTFSI electrolyte is discussed and concluded as a combination of two bands. To support this assignment, the spectrum of PEO$_{10}$LiTFSI is subtracted from the spectrum of cr-PEO$_{10}$LiTFSI, as shown in Figure S3 (Supporting Information). The subtraction also indicates that the band ≈1652 cm^{-1} is a combination of two bands: one from the ν(C═O) band ≈1658 cm^{-1} of BP, and another from ≈1647 cm^{-1} of the PEO$_{10}$LiTFSI complex. As discussed later in this study, the evolution of these bands provides detailed insights into the interfacial processes during Li plating.

2.3. Knowledge Transfer to Spectro-Electrochemical Cell/Operando Characterization of cr-PEO$_{10}$LiTFSI Electrolyte

Before conducting the operando ATR-FTIR spectroscopy investigation, it is crucial to achieve reliable and reproducible Li plating/stripping processes in the spectro-electrochemical cell. The resulting voltage profile, which contains the crosslinked PEO electrolyte (cr-PEO$_{10}$LiTFSI), is shown in **Figure 3**.

The first plating step exhibits a stable overvoltage plateau within the range from −0.06 to −0.20 V after initiation for 2 h. The subsequent stripping exhibits a higher overvoltage plateau of 0.21 to 0.43 V. Notably, the stripping plateau is maintained for only one-quarter of the plating plateau, resulting in a CE of just 22%. The low CEs observed in the anode-free configuration are likely due to the existing of minor defects or irregularities on copper surface that act as nucleation points for Li deposition, causing uneven plating and promoting the growth of dendritic structures. The interphase between the deposited Li metal and the solid electrolyte may not be stable, resulting in side reactions at the interface, and contributing to the irreversible Li loss.[56] During the plating/stripping process, the interfacial ATR-FTIR spectra of the cr-PEO$_{10}$LiTFSI electrolyte are recorded at the corresponding potentials, and the resulting full spectra are shown in Figure S4 (Supporting Information).

The full operando spectra collected at 25 and 60 °C during the first plating/stripping cycle under 60 °C are shown in Figure S4a (Supporting Information). As depicted in this figure, no distinct band variations can be observed, however, the overall band intensity slightly decreased, which may stem

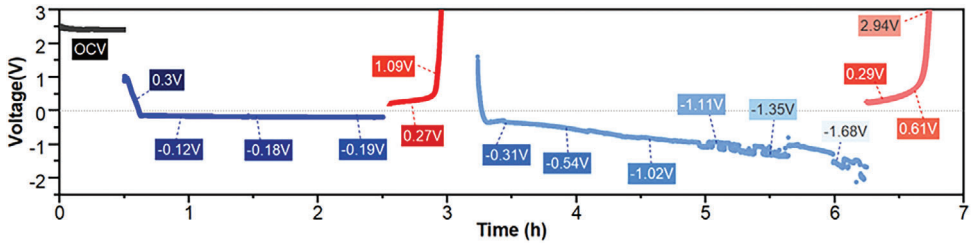

Figure 3. Voltage versus time profile of Li plating/ stripping at current density of 0.05 mA cm^{-2} in the spectro-electrochemical cell with copper mesh current collector containing cr-PEO_{10}LiTFSI electrolyte at 60 °C.

from the degradation of electrolytes or the deposition of Li metal.

The extracted characteristic regions from the obtained operando ATR-FTIR full spectra are shown in **Figure** 4a–c. Bands are highlighted with their corresponding wavenumbers and vibrational modes, and different colors of the bands represent different band origins. Green, red, purple, and yellow region represent the bands corresponding to PEO, LiTFSI, benzophenone, and new decomposition products, respectively.

When comparing the spectra obtained at 25 and 60 °C, the band ≈843 cm^{-1} in Figure 4c, attributed to $\delta(CH_2)$ from the crystalline PEO, is visible at 25 °C, however, this band diminishes at 60 °C and a broad band ≈847 cm^{-1} appears. This change suggests a decrease in the level of PEO crystallinity due to the higher temperature and better incorporation of LiTFSI and BP in the PEO matrix.

As shown in Figure 3, the overvoltage increases from −0.28 to ≈−2.00 V with increasing plating time in the second plating cycle. The second plating time lasts almost 3 h before reaching an overvoltage of −2.00 V, followed by a stripping period, which is less than a quarter of the plating time, corresponding to CE of just 14%. In addition, the voltage profile exhibits increasing noise after surpassing an overvoltage of −1.11 V, indicating severe occurrence of side reactions.

Full spectra of the second plating/stripping cycle are shown in Figure S4b (Supporting Information), and the extracted characteristic regions from the obtained operando ATR-FTIR full spectra are shown in Figure 4d–f. Contrary to the first cycle, notable changes in the IR bands are observed during the second

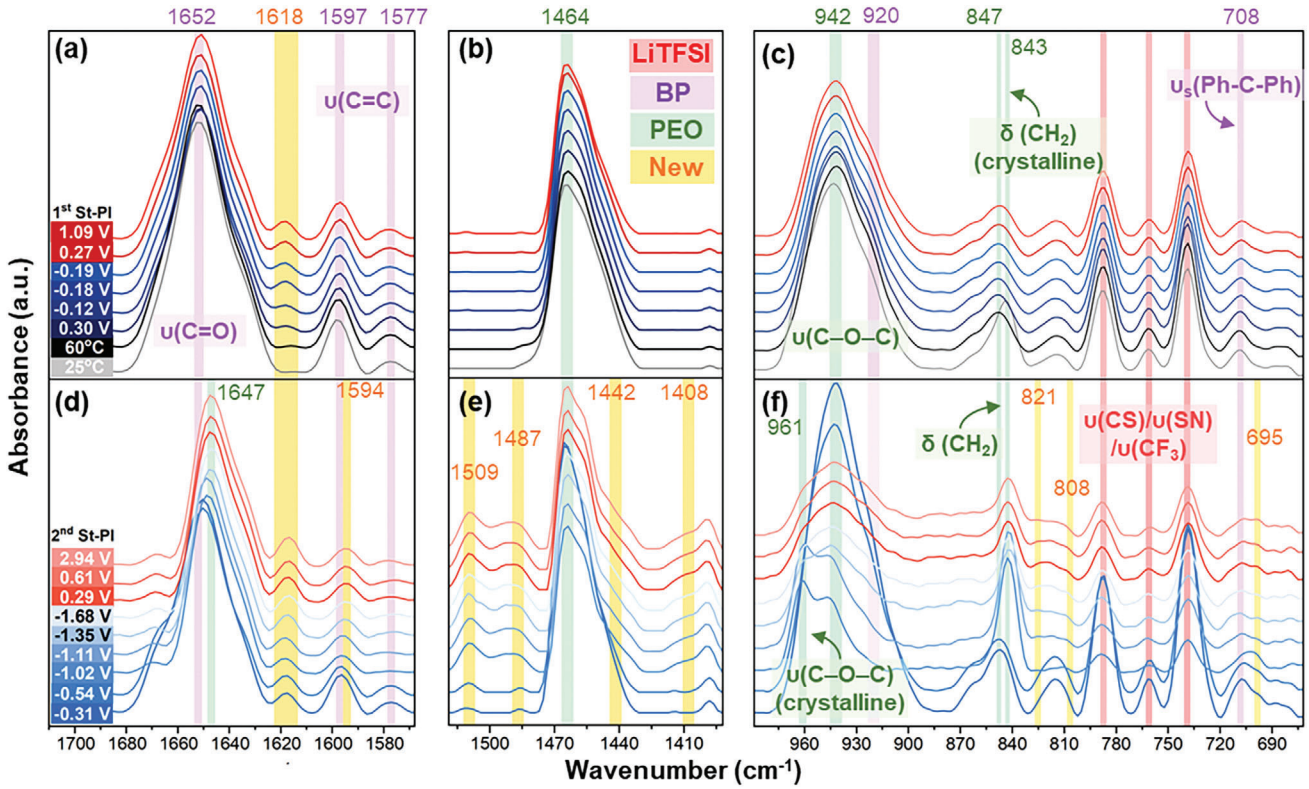

Figure 4. Operando ATR-FTIR spectra of the cell containing cr-PEO_{10}LiTFSI electrolyte in contact with copper mesh during Li plating/stripping. The blue spectra represent the plating process, and the red spectra correspond to the stripping process. Dark to light color relates to the time of the procedure. a–c) Spectra from the first plating/stripping cycle and d–f) spectra from the second plating/stripping cycle.

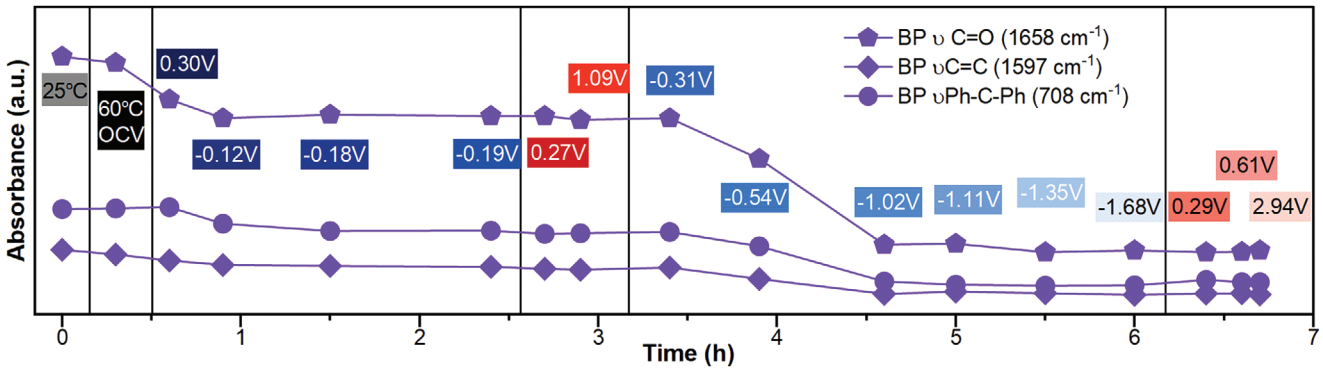

Figure 5. IR absorbance intensity of representative bands (ν(C═O) at 1658 cm^{-1} and ν(C═C) at 1597 and 1577 cm^{-1}) related to benzophenone in cr-PEO$_{10}$LiTFSI electrolyte before (25 °C) and during the electrochemical process of plating/stripping with current density of 0.05 mA cm^{-2} at 60 °C in the spectrochemical cell (Li|Cu mesh).

plating step shown in Figure 4d–f, especially when the plating overvoltage exceeds −1.02 V. As shown in Figure 4d, the band ≈1652 cm^{-1}, mentioned earlier to consist of two separate bands, decreases in intensity and shifts to 1647 cm^{-1} during the second plating. This suggests that one of the peaks, corresponding to ν(C═O) stretch from BP ≈1658 cm^{-1} is disappearing, while the band ≈1647 cm^{-1}, associated with the PEO$_{10}$LiTFSI complex, remains. To validate our assumption, we performed IR spectrum subtraction between the OCV spectrum and the spectrum obtained during the second plating at -1.68 V, as shown in Figure S5a (Supporting Information). The resulting subtraction spectrum reveals a band ≈1658 cm^{-1}, which closely resembles the spectrum of bulk BP. This indicates that the shift of the band from 1652 to 1647 cm^{-1} during second plating is caused by the disappearance of the band ≈1658 cm^{-1}, indicating a reduction of ν(C═O) bond from BP within the electrolyte at the interface. In addition to the spectrum subtraction method, an additional experiment was conducted to further confirm the assumption of BP degradation. In this experiment, an electrolyte composed of tetraglyme and 5 wt% of BP was prepared and electrochemically investigated in a coin cell. Tetraglyme resembles PEO structure, being an ideal benchmark for this comparison, thanks to its liquid composition enabling more direct IR measurement of IR. Following the same electrochemical procedure used previously in Figure 3, post-mortem ATR-FTIR spectroscopy measurements were conducted to examine the changes in the electrolyte composition. The detailed experiment procedure and discussion of the results can be found in the paragraph under Figure S5b (Supporting Information). The observed decrease in the ν(C═O) bands of BP in the aged electrolyte containing tetraglyme, further supports the assumption of BP degradation. Furthermore, the reduced intensity of the bands ≈1599 and 1578 cm^{-1}, attributed to ν(C—C) vibration of BP's phenyl groups, was noted after the electrochemical process. This observation aligns with the operando IR results shown in Figure 4d, where the bands at 1597 and 1577 cm^{-1} similarly decrease. Moreover, the band ≈1597 cm^{-1} in Figure 4d appears to exhibit either a small shift or a new band ≈1594 cm^{-1}. Additionally, bands corresponding to ν(Ph-C-Ph) vibration at ≈708 and 920 cm^{-1} also decreased as the overvoltage dropped below −1.00 V. The decomposition process of BP, as a function of IR absorbance intensity of distinct bands in Figure 4 versus time during the first and second plating/stripping, is more clearly illustrated in **Figure 5**. This Figure shows that BP began decomposing during the second plating, with more pronounced decomposition occurring once the overvoltage exceeded −1.00 V.

The reactions of BP crosslink-initiators during the electrochemical processes are rarely discussed due to their relatively low concentration in the electrolyte, typically ranging from 1 to 8 wt%.[28,57–60] However, in the ATR-FTIR spectra in Figure 4, the characteristic bands of BP: such as ν(C═O) at 1658 cm^{-1} and ν(C═C) at 1597 and 1577 cm^{-1} — are clearly observed even at a concentration of just 5 wt% in the electrolyte. As shown in Figure 4d, these BP bands decrease and eventually vanish during the second plating step, indicating the degradation of BP.

BP-like compounds are commonly used as the crosslinking initiator in polymer electrolytes, but they can also be used as indicator for the presence of alkali metals like Li.[61] When BP interacts with Li metals, Li ions are complexed by BP, as depicted in **Scheme 1**. In this complex, BP exists in a negatively charged form, where the typical (C═O) double bond is replaced by a (C—O) single bond. This leads to a color change of the solution from colorless to blue. Furthermore, an excess of alkali metals can intensify the color change to purple, further increasing the negativity of BP.[62] However, exposure of the complex

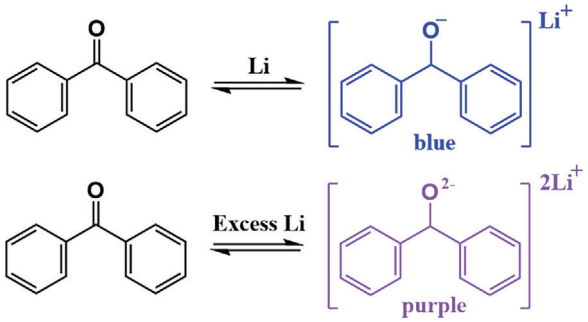

Scheme 1. Benzophenone reacts with alkali metals like Li metal and forms the complex. Excess Li further reduces benzophenone to a complex with two Li ions, which is a more unstable form that would further lead to decomposition.

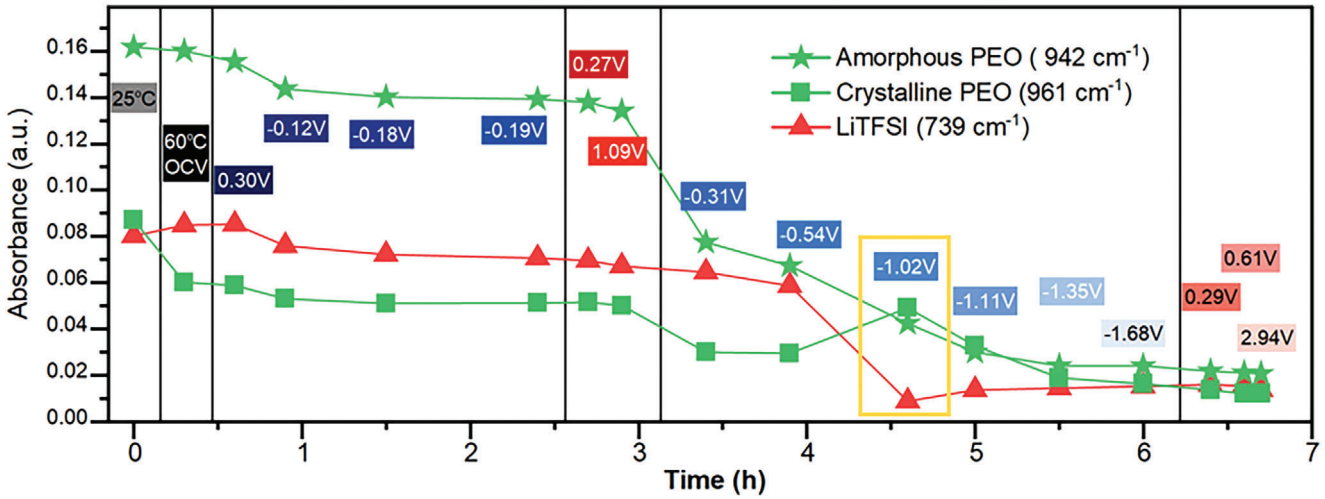

Figure 6. Absorbance intensity of bands related to crystalline/amorphous PEO and LiTFSI in cr-PEO$_{10}$LiTFSI electrolyte before (25 °C) and during the electrochemical process of plating/stripping with current density of 0.05 mA cm^{-2} at 60 °C in the spectrochemical cell (Li|Cu mesh).

to oxygen and moisture can reverse these changes, restoring the original state of BP.

It can be hypothesized that during the continuous plating of Li metal, BP may form a complex with Li, leading to a decrease in the IR intensity of the band corresponding to the C═O bond, while the IR intensity of the C═C bond vibration of phenyl groups remains relatively stable. However, as Li metal plating progresses and dendrites form, regarded as excess Li metal for BP at the interface, the complex may transition to the form of $[Ph_2CO]^{2-}$. This transition could lead to increased Li consumption and instability of the compound.

To summarize, the formation of the Li-coordinated complex can be inferred from the decreasing intensity of the IR band corresponding to the ν(C═O) bond vibration. Besides, the raised instability of BP when in contact with excess Li metal, might trigger the degradation of the compound. This degradation is evidenced by the shift in the ν(C═C) vibration in the region ≈1598 and 1577 to 1594 cm^{-1}.

Regarding other bands shown in Figure 4, the band ≈942 cm^{-1}, assigned to vibration ν_s(C—O—C) of PEO, decreases in intensity over time in the second plating step. In addition, a new band ≈961 cm^{-1} arises when the voltage drops below −1.00 V. As shown in Figure S2 (Supporting Information), pure PEO exhibits a band ≈961 cm^{-1}, indicating the crystalline PEO. However, the band becomes broader when LiTFSI and BP are added, suggesting a decrease in PEO crystallinity and transition to amorphous PEO.[51] **Figure 6** shows the absorbance intensity profile of the bands related LiTFSI and crystalline/amorphous PEO. It is evident that the band intensity of the crystalline PEO decreased as the temperate rises from 25 to 60 °C. Furthermore, the band intensity of LiTFSI decreased when voltage falls below −1.00 V, exactly correlating with an increase in the crystalline PEO band intensity. It is even possible that the degradation processes might have already occurred within the range from −0.54 to −1.02 V. According to the theoretical calculations of the electrochemical stability window for PEO, LiTFSI, and their mixture, presented by Cleber et al., both PEO and LiTFSI individually exhibit wide stability windows. However, when combined, the mixture results in a reduced electrochemical stability window.[63] This indicates that PEO with LiTFSI may be less stable during electrochemical processes than assumed, potentially leading to side reactions, especially during extensive lithium deposition where interfacial reactions are likely exacerbated. It can be observed in the IR results that LiTFSI bands were already significantly decreased in intensity when the voltage dropped from −0.54 to below −1.02 V. Furthermore, the band intensity of amorphous PEO gradually decreased during this period, indicating that, as the components in the electrolyte approach their theoretical electrochemical stability window limit, the degradation occurred and further formed the side reaction products.

The phenomenon is also observed for the $\delta(CH_2)$ band of PEO ≈847 cm^{-1}, which shifts to 843 cm^{-1}. This implies that the composition of the electrolyte composition at the Li|PEO interface changes during the second plating process, resulting in increased crystallinity of PEO at the interface. The increase in the crystallinity of PEO also lead to reduced Li ion conductivity (high impedance) at the interface, which contributes to the severe rise in the overvoltage, as shown in Figure 3.

Moreover, new bands can be identified in Figure 4d,e ≈1408, 1442, 1487, 1509, and 1618 cm^{-1}. These bands cannot be assigned to the pristine electrolyte species and, therefore, likely originate from the degradation of electrolyte components at the interface.

To identify the origin of the new bands and solely investigate the degradation of the PEO polymer and LiTFSI salt, an additional operando IR investigation is conducted using PEO$_{10}$LiTFSI as the electrolyte membrane (without any crosslink-initiator). Here, the same plating/stripping procedure and operando IR measurement in Figures 3 and 4 are used. The voltage profile of the Li plating/stripping is shown in Figure S6 (Supporting Information), and the full and extracted spectra in Figures S7 and S8 (Supporting Information), respectively, along with the detailed discussion of band assignments.

Comparing the voltage profiles of the second plating step of the cells of PEO$_{10}$LiTFSI (Figure S6, Supporting Information) and cr-PEO$_{10}$LiTFSI (Figure 3) electrolyte, different increase

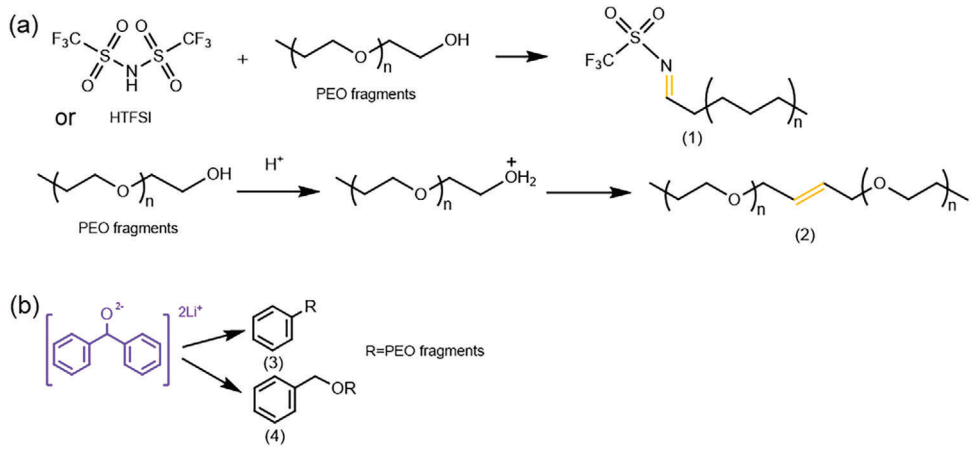

Scheme 2. a) Postulated degradation compounds of PEO and TFSI anion: one formed from HTFSI and PEO fragment, resulting in the degradation compound containing C═N bond as shown in compound 3. The other one formed from PEO fragments, resulting in the degradation compound containing C═C bond as shown in compound 4. The C═N and C═C bonds are highlighted in orange. b) Postulated degradation compounds of BP: the unstable BP reacts with PEO fragments (-R), forming the compounds consisting of PEO attached to a benzene ring as shown in compound 1 and 2.

rates of the overvoltage are observed. Whereas the cell with cr-PEO_{10}LiTFSI reached the overvoltage of −2.00 V after 3 h, the cell with PEO_{10}LiTFSI reached this overvoltage within 2 h. This difference may be attributed to the crosslinking sites of the polymer (cr-PEO_{10}LiTFSI) that deferred the decomposition of the electrolytes, leading to a longer lifetime. The comparison of the electrochemical stabilities of cr-PEO_{10}LiTFSI and PEO_{10}LiTFSI electrolytes can also be observed through voltage sweep measurement, shown in Figure S9 (Supporting Information) with a detailed discussion. A series of voltage sweep measurements were performed, scanning from OCV to −0.10 V, and then returning to 0.10 V. With each cycle, the upper and lower cut-off voltages were incrementally increased by 0.10 V to assess the electrochemical stability of the two materials. In the fourth cycle between 0.40 and −0.40 V (Figure S9d, Supporting Information), noisy data points were observed for the PEO_{10}LiTFSI electrolyte, which indicates the instability of the electrolyte. This aligns with the earlier and more pronounced polarization phenomena observed during the plating stripping process in Figure 3. It is shown in Figure S8 (Supporting Information) that, except for bands corresponding to BP, other band changes of PEO_{10}LiTFSI cell are similar to spectra of cr-PEO_{10}LiTFSI cell in Figure 4. Some increasing bands ≈1618, 1509, 1487, and 1442 cm^{-1} are both observed in the spectra of the cr-PEO_{10}LiTFSI electrolyte (Figure 4) and PEO_{10}LiTFSI electrolyte (Figure S8, Supporting Information), suggesting that these bands are more likely related to PEO or LiTFSI vibrational modes. According to the possible mechanism of PEO and LiTFSI degradation proposed by Faglioni et al., HTFSI could be formed by taking the hydrogen from the carbon on PEO.[64] Therefore, the band ≈1618 cm^{-1}, which rises during the plating process, may indicate PEO decomposition and the formation of Li alkoxide species with a C═C bond component.[52] Another potential degradation products include shorter PEO chains reacting with HTFSI and forming degradation products containing C═N groups.[64,65] The calculated vibrational frequency for ν(C═N) bond at 1619 cm^{-1}, as shown in Table S6 (Supporting Information), corresponds closely to the experimental wavenumber of the band ≈1618 cm^{-1}. The structures of the postulated compounds are shown as compound 1 and 2 in **Scheme 2**. Moreover, the bands ≈1442 and 1487 cm^{-1} are often assigned to ν(C—O) of lithiated carbonate species, like Li_2CO_3 or semi-carbonates.[51] The band ≈1509 cm^{-1} is often assigned to $\delta(CH_2)$, which can originate from the above-mentioned PEO degradation.[66,67] This assignment is supported by the observation that the intensity of the band ≈1464 cm^{-1}, attributed to PEO, decreases while the bands ≈1509 cm^{-1} grow. Additionally, no new band arises ≈1400 cm^{-1} in Figure S8e (Supporting Information) (spectra of PEO_{10}LiTFSI) in contrast to the spectra of cr-PEO_{10}LiTFSI in Figure 4e. The absence of this band in the spectra of the PEO_{10}LiTFSI suggests that this band is attributed to the BP-related degradation product. Furthermore, a new band is observed at lower wavelengths ≈695, 808, and 821 cm^{-1}. These bands along with the band ≈1408 cm^{-1} can correspond to a compound consisting of PEO attached to a benzene ring, as the proposed compound 3 and 4 in Scheme 2. We speculate that the attachment of an aliphatic group to a benzene ring decreases the electron density of the ring, shifting the vibrational frequency to lower wavelengths. To support this claim, the calculated IR spectrum of this component (in Tables S7 and S8, Supporting Information) exhibits IR active bands at 1400, 808, 821, and 695 cm^{-1}.

In light of these findings, a scheme illustrating the formation of putative degradation products at the interface of the electrolyte and Li metal is proposed in **Figure 7**. One notable degradation phenomenon would be corresponding to BP, formed at the interface as through the coordination of benzene with the PEO fragments. Other possible degradation products include the PEO-TFSI, PEO fragments, -TFSI fragments, or semi-carbonates, which are derived from the attack or degradation of HTFSI and degradation of PEO. Overall, during the plating process, Li metal is continuously and unevenly deposited onto the copper substrate, and reactions occur between the deposited Li metal and the cr-PEO_{10}LiTFSI electrolyte at the interface. The degradation mechanism at the interface is proposed and summarized as follows:

The degradation of BP is attributed to its interaction with deposited Li metal, forming unstable intermediates, which likely

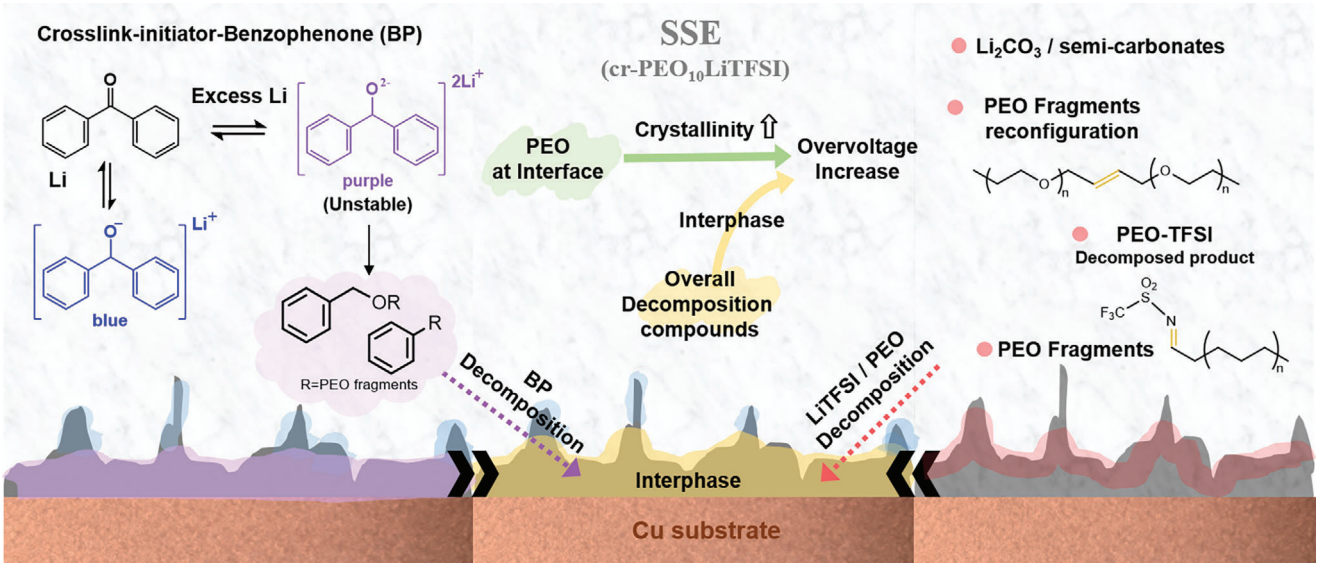

Figure 7. Schematic illustration of the potential degradation products and mechanism formed at the interface between the electrolyte and the deposit Li metal captured via operando ATR-FTIR spectroscopy. The left scheme illustrates the decomposition of the crosslink-initiator (BP), and the right scheme illustrates the decomposition corresponding to PEO and LiTFSI, and consequently, the overall decomposition results in increase of crystalline PEO as shown in the middle scheme.

results in further decomposition, and engages in the formation of the interphase. Regarding LiTFSI and PEO, the degradation is driven by exceeding their electrochemical stability windows, leading to the formation of an interphase, consisting of decomposition compounds. As BP and LiTFSI degrade at the interface, the proportions of BP and LiTFSI remaining in the electrolyte at the interface are greatly reduced. As mentioned previously, the addition of BP and LiTFSI plays a crucial role in reducing the crystallinity of PEO. Consequently, their decomposition results in an increase in PEO crystallinity, due to a reduced concentration.

3. Conclusion

This study presents the successful application of our developed operando ATR-FTIR spectroscopy method toward investigating the interphase between Li metal and polymer electrolytes in solid-state batteries, employing standard PEO polymer electrolyte as a proof of concept. The operando IR spectra indicated the degradation of electrolyte components during the plating/stripping processes, particularly under conditions of high polarization or overvoltage.

Notably, bands assigned to the crosslink-initiator benzophenone (BP) showed distinct changes during the Li plating/stripping process, indicating the degradation of BP at the interface between the electrolyte and plated Li. This finding is of great importance, as reactions involving minor electrolyte components are often overlooked due to their low concentration in the electrolyte. Despite the clear evidence of BP degradation, it cannot be definitively concluded that BP leads to adversely affects. In fact, BP-containing electrolytes (cr-PEO_{10}LiTFSI) demonstrated a longer Li plating/stripping plateau, likely due to the enhanced mechanical strength provided by the crosslinked sites. The operando IR investigations indicate that BP degradation predominantly occurs under conditions of excessive Li deposition. Furthermore, bands corresponding to electrolyte degradation products were identified in the operando ATR-FTIR spectra during Li plating. Furthermore, a transition from amorphous to crystalline PEO was observed as BP and LiTFSI were consumed. Based on these findings, we proposed potential degradation products and provided insight into the phenomenon occurring at the interface of Li metal and cr-PEO_{10}LiTFSI electrolyte.

The successful development and implementation of the operando ATR-FTIR spectroscopy and the established techniques validating its developmental promise and its potential application as a reliable method for exploring the interphase formed between polymer electrolyte and Li metal. Allowing a straightforward, systematic investigation of interfacial reactions and interphase formation mechanisms in batteries with various types of polymer electrolytes, offering crucial knowledge-based and advanced insights to support the development of high-performance future solid-state batteries.

4. Experimental Section

Membranes Preparation: Polyethylene oxide (PEO, MW = 5 M, Sigma–Aldrich) and benzophenone (BP, 99%, Sigma–Aldrich) were dried under reduced atmosphere at 40 °C for 48 h. Li bis(trifluoromethanesulfonyl) imide (LiTFSI, battery grade, E-Lyte Innovation) was dried under reduced pressure at 100 °C for 48 h.

For the preparation of cr-PEO_{10}LiTFSI membranes, PEO and LiTFSI with a fixed molar ratio of 10:1 were mixed with 5 wt% of BP, sealed in a pouch bag under reduced pressure, and heated for 12 h at 100 °C. After hot pressing with a pressure of 100 bar at 100 °C, the 0.20 mm thick electrolyte membrane was cured for 5 min by UV radiation (UVACUBE 100, Dr. Hönle AG).

For preparation of PEO_{10}LiTFSI membranes, PEO and LiTFSI were mixed with a fixed molar ratio of 10:1 and sealed in a pouch bag under

reduced pressure, heated for 12 h at 100 °C, and then hot pressed under 100 bar at 100 °C, Afterward, a 0.20 mm thick electrolyte membrane was obtained.

Spectro-Electrochemical Cell Configuration: The spectro-electrochemical cell employed in this study is based on a previously reported cell from the group.[53] For temperature control, the cell was modified to facilitate its compatibility with a high-precision heating cartridge (40 W, 24 V, E3D) which supports a maximum temperature of 300 °C, and temperature sensor (PT-100, E3D), which is connected to a temperature control system (ESM-4420, EMKO). The applied Li metal counter electrode has a thickness of 0.50 mm, and the Copper mesh (AOT ELEC, China) working electrode has a thickness of 12 µm, pore size of 0.80 mm, and hole spacing of 1.50 mm. The surface area of a 1 cm diameter copper mesh is roughly 80% of equivalent copper foil.

Coin Cell Configuration: All coin cells were assembled in a two-electrode coin cell setup (CR2032) in a dry room (dew point <−50 °C, 0.02% moisture content). For CR2032 coin cells, stainless-steel upper and bottom caps and spacers of 0.50 and 1.00 mm thickness were employed, other components were same as in the spectroelectrochemical cell, shown in Figure 2.

Electrochemical Procedure-Parameters: Electrochemical investigations of coin cells were performed with the Biologic VMP3 Potentiostat/Galvanostat/FRA instrument connected to a 60 °C constant temperature oven (Memmert), where the cells were placed for testing. Initially, an OCV step was conducted for 2 h to reach thermal equilibrium, and then Li plating/stripping processes were conducted for 2 h each at the respective current densities, with a 15-min rest period between each cycle.

Li plating/stripping processes on spectro-electrochemical cells were measured on a potentiostat/galvanostat PGSTAT204 (Metrohm) controlled by NOVA .1 software (Metrohm). The inner heated unit was heated to a constant temperature of 60 °C. Initially, an OCV step was conducted for 30 min to reach thermal equilibrium, and then a current density of 0.05 mA cm^{-2} for Li plating/stripping was applied.

ATR-FTIR Instrument: The operando ATR-FTIR spectroscopy measurements were conducted on an Invenio-R (Bruker) with a mercury–cadmium–telluride (MCT) detector, equipped with the VeeMAX III automatic variable angle specular reflection accessory (PikeTechnologies, US) located in a N_2 flushed glovebox. The cell is attached to a ZnSe ATR crystal (Bruker) as reflective crystal to the in-house build spectro-electrochemical cell shown in Figure 1. The spectro-electrochemical cell was designed with the software Inventor Professional 2022 (Autodesk, US), and 3D-printed in a Mars 3 3D-printer (Elegoo, US) using Composite-X resin (Liqcreate, Netherlands).

The ATR-FTIR spectroscopy measurement of reference bulk materials in Figure S2 (Supporting Information) was conducted on the above-mentioned ATR-FTIR spectrometer using a diamond crystal ATR unit (Platinum ATR, Bruker). The spectra were recorded at 25 °C.

Each spectrum was obtained by accumulating 64 samples and 32 background scans, and the resolution of the spectrum was 4 cm^{-1}. Besides, all spectra were processed with extended background correction and H_2O corrections.

The band correlation analysis was conducted by adding the value before, after and the maximum value of the absorbance of each band, as the representation of each electrolyte material component.

Computational Details: Density functional theory (DFT) calculations were carried out using the Gaussian16 package. The molecular structures were optimized using B3LYP DFT functional and the 6–311++G(3df, 2p) basis set. In order to mimic the effect of a surrounding electrolyte, a solvation model with the parameters for diethyl ether was used, as it shows a similar dielectric constant $\varepsilon = 4.24$, similar to PEO.[64] After geometry optimization, the calculated IR frequencies and intensities of the molecular structures of the components (LiTFSI, PEO, Benzophenone, and some possible degradation products) were used to support the band assignment of the ATR-FTIR spectra. The results with a frequency scaling factor of 1 and 0.98 and full computational results are shown in Supporting Information with assignments.

Supporting Information

Supporting Information is available from the Wiley Online Library or from the author.

Acknowledgements

Financial support from the German Federal Ministry for Education and Research within the project "EFoBatt" (grant number 13XP5129) is gratefully acknowledged.

Open access funding enabled and organized by Projekt DEAL.

Conflict of Interest

The authors declare no conflict of interest.

Data Availability Statement

The data that support the findings of this study are available from the corresponding author upon reasonable request.

Keywords

anode-free electrode, interphase characterization, operando ATR-FTIR, solid-state batteries, solid-state polymer electrolyte

Received: October 3, 2024
Revised: December 5, 2024
Published online: December 29, 2024

[1] M. S. Whittingham, *Proc. IEEE* **2012**, *100*, 1518.
[2] J.-M. Tarascon, *Philos. Trans. R. Soc., A* **2010**, *368*, 3227.
[3] S. Kim, G. Park, S. J. Lee, S. Seo, K. Ryu, C. H. Kim, J. W. Choi, *Adv. Mater.* **2023**, *35*, 2206625.
[4] P. Shi, X. Q. Zhang, X. Shen, R. Zhang, H. Liu, Q. Zhang, *Adv. Mater. Technol.* **2020**, *5*, 1900806.
[5] C. Heubner, S. Maletti, H. Auer, J. Hüttl, K. Voigt, O. Lohrberg, K. Nikolowski, M. Partsch, A. Michaelis, *Adv. Funct. Mater.* **2021**, *31*, 2106608.
[6] Z. Xie, Z. Wu, X. An, X. Yue, J. Wang, A. Abudula, G. Guan, *Energy Storage Mater.* **2020**, *32*, 386.
[7] B. Wu, C. Chen, L. H. Raijmakers, J. Liu, D. L. Danilov, R.-A. Eichel, P. H. Notten, *Energy Storage Mater.* **2023**, *57*, 508.
[8] Y.-C. Hsieh, M. Leißing, S. Nowak, B.-J. Hwang, M. Winter, G. Brunklaus, *Cell Rep. Phys. Sci.* **2020**, *1*, 100139.
[9] W. Xu, J. Wang, F. Ding, X. Chen, E. Nasybulin, Y. Zhang, J.-G. Zhang, *Energy Environm. Sci.* **2014**, *7*, 513.
[10] T. Placke, R. Kloepsch, S. Dühnen, M. Winter, *J. Solid State Electrochem.* **2017**, *21*, 1939.
[11] Y. Guo, H. Li, T. Zhai, *Adv. Mater.* **2017**, *29*, 1700007.
[12] H. Wu, H. Jia, C. Wang, J. G. Zhang, W. Xu, *Adv. Energy Mater.* **2021**, *11*, 2003092.
[13] Y. Chen, Y. Kang, Y. Zhao, L. Wang, J. Liu, Y. Li, Z. Liang, X. He, X. Li, N. Tavajohi, *J. Energy Chem.* **2021**, *59*, 83.
[14] D.-H. Liu, Z. Bai, M. Li, A. Yu, D. Luo, W. Liu, L. Yang, J. Lu, K. Amine, Z. Chen, *Chem. Soc. Rev.* **2020**, *49*, 5407.
[15] T. T. Ingber, M. M. Bela, F. Püttmann, J. F. Dohmann, P. Bieker, M. Börner, M. Winter, M. C. Stan, *J. Mater. Chem. A* **2023**, *11*, 17828.

[16] J. R. Nair, L. Imholt, G. Brunklaus, M. Winter, *Electrochem. Soc. Interface* **2019**, *28*, 55.
[17] C. Zor, S. J. Turrell, M. S. Uyanik, S. Afyon, *Adv. Energy Sustainability Res.* **2023**, *5*, 2300001.
[18] Z. Song, F. Chen, M. Martinez-Ibañez, W. Feng, M. Forsyth, Z. Zhou, M. Armand, H. Zhang, *Nat. Commun.* **2023**, *14*, 4884.
[19] Y. Jiang, X. Yan, Z. Ma, P. Mei, W. Xiao, Q. You, Y. Zhang, *Polymers* **2018**, *10*, 1237.
[20] E. Quartarone, P. Mustarelli, A. Magistris, *Solid State Ionics* **1998**, *110*, 1.
[21] O. Borodin, G. D. Smith, *Macromolecules* **2006**, *39*, 1620.
[22] T. T. Ingber, D. Liebenau, M. Biedermann, M. Kolek, D. Diddens, H.-D. Wiemhöfer, A. Heuer, M. Winter, P. Bieker, *J. Electrochem. Soc.* **2021**, *168*, 070559.
[23] M. Marzantowicz, J. Dygas, F. Krok, J. Nowiński, A. Tomaszewska, Z. Florjańczyk, E. Zygadło-Monikowska, *J. Power Sources* **2006**, *159*, 420.
[24] M. Doytcheva, D. Dotcheva, R. Stamenova, A. Orahovats, C. Tsvetanov, J. Leder, *J. Appl. Polym. Sci.* **1997**, *64*, 2299.
[25] J. Chattopadhyay, T. S. Pathak, D. M. Santos, *Polymers* **2023**, *15*, 3907.
[26] M. Falco, C. Simari, C. Ferrara, J. R. Nair, G. Meligrana, F. Bella, I. Nicotera, P. Mustarelli, M. Winter, C. Gerbaldi, *Langmuir* **2019**, *35*, 8210.
[27] O. Garcia-Calvo, N. Lago, S. Devaraj, M. Armand, *Electrochim. Acta* **2016**, *220*, 587.
[28] B. Rupp, M. Schmuck, A. Balducci, M. Winter, W. Kern, *Eur. Polym. J.* **2008**, *44*, 2986.
[29] J. Weidelt, J. R. Nair, D. Diddens, W. Zhang, F. Pfeiffer, T. de Oliveira Schneider, M. Meinert, T. Hiraoka, L. Nesterov, M. Baghernejad, *J. Phys. Chem. C* **2024**, *128*, 6868.
[30] E. Peled, S. Menkin, *J. Electrochem. Soc.* **2017**, *164*, A1703.
[31] U. S. Meda, L. Lal, M. Sushantha, P. Garg, *J. Energy Storage* **2022**, *47*, 103564.
[32] H. Adenusi, G. A. Chass, S. Passerini, K. V. Tian, G. Chen, *Adv. Energy Mater.* **2023**, *13*, 2203307.
[33] P. Verma, P. Maire, P. Novák, *Electrochim. Acta* **2010**, *55*, 6332.
[34] X. Shan, Y. Zhong, L. Zhang, Y. Zhang, X. Xia, X. Wang, J. Tu, *J. Phys. Chem. C* **2021**, *125*, 19060.
[35] O. B. Chae, B. L. Lucht, *Adv. Energy Mater.* **2023**, *13*, 2203791.
[36] B. Li, Y. Chao, M. Li, Y. Xiao, R. Li, K. Yang, X. Cui, G. Xu, L. Li, C. Yang, *Electrochem. Energy Rev.* **2023**, *6*, 7.
[37] B. Wu, S. Wang, J. Lochala, D. Desrochers, B. Liu, W. Zhang, J. Yang, J. Xiao, *Energy Environ. Sci.* **2018**, *11*, 1803.
[38] C. Xu, B. Sun, T. Gustafsson, K. Edström, D. Brandell, M. Hahlin, *J. Mater. Chem. A* **2014**, *2*, 7256.
[39] C. Sångeland, G. Hernández, D. Brandell, R. Younesi, M. Hahlin, J. Mindemark, *ACS Appl. Mater. Interfaces* **2022**, *14*, 28716.
[40] M. Le Granvalet-Mancini, T. Hanrath, D. Teeters, *Solid State Ionics* **2000**, *135*, 283.
[41] B. Sun, C. Xu, J. Mindemark, T. Gustafsson, K. Edström, D. Brandell, *J. Mater. Chem. A* **2015**, *3*, 13994.
[42] M. M. Amaral, C. G. Real, V. Y. Yukuhiro, G. Doubek, P. S. Fernandez, G. Singh, H. Zanin, *J. Energy Chem.* **2023**, *81*, 472.
[43] J.-H. Cheng, A. A. Assegie, C.-J. Huang, M.-H. Lin, A. M. Tripathi, C.-C. Wang, M.-T. Tang, Y.-F. Song, W.-N. Su, B. J. Hwang, *J. Phys. Chem. C* **2017**, *121*, 7761.
[44] H. Marceau, C.-S. Kim, A. Paolella, S. Ladouceur, M. Lagacé, M. Chaker, A. Vijh, A. Guerfi, C. M. Julien, A. Mauger, *J. Power Sources* **2016**, *319*, 247.
[45] F. Pfeiffer, D. Diddens, M. Weiling, M. Baghernejad, *ACS Appl. Mater. Interfaces* **2023**, *15*, 6676.
[46] F. Pfeiffer, D. Diddens, M. Weiling, L. Frankenstein, S. Kühn, I. Cekic-Laskovic, M. Baghernejad, *Adv. Energy Mater.* **2023**, *13*, 2300827.
[47] M. B. Dixit, J.-S. Park, P. Kenesei, J. Almer, K. B. Hatzell, *Energy Environ. Sci.* **2021**, *14*, 4672.
[48] R. N. Samajdar, S. Marchesini, S. A. Brown, S. D. Robertson, K. R. Paton, A. J. Pollard, A. J. Wain, *ACS Energy Lett.* **2023**, *8*, 1864.
[49] M. Weiling, F. Pfeiffer, M. Baghernejad, *Adv. Energy Mater.* **2022**, *12*, 2202504.
[50] O. Chusid, Y. Gofer, D. Aurbach, M. Watanabe, T. Momma, T. Osaka, *J. Power Sources* **2001**, *97*, 632.
[51] X. He, J. M. Larson, H. A. Bechtel, R. Kostecki, *Nat. Commun.* **2022**, *13*, 1398.
[52] K. Yamada, H. Tsutsumi, Y. Katayama, *Energy Technol.* **2023**, *11*, 2201286.
[53] M. Weiling, C. Lechtenfeld, F. Pfeiffer, L. Frankenstein, D. Diddens, J. F. Wang, S. Nowak, M. Baghernejad, *Adv. Energy Mater.* **2024**, *14*, 2303568.
[54] L. Zhang, B. L. Chaloux, T. Saito, M. A. Hickner, J. L. Lutkenhaus, *Macromolecules* **2011**, *44*, 9723.
[55] N. A. Stolwijk, M. Wiencierz, C. Heddier, J. Kösters, *J. Phys. Chem. B* **2012**, *116*, 3065.
[56] H. Fan, C. Gao, H. Jiang, Q. Dong, B. Hong, Y. Lai, *J. Energy Chem.* **2020**, *49*, 59.
[57] R. S. Teixeira, R. J. Correa, A. Belvino, R. S. Nascimento, *J. Appl. Polym. Sci.* **2013**, *130*, 2458.
[58] S. H. Siyal, M. Li, H. Li, J.-L. Lan, Y. Yu, X. Yang, *Appl. Surf. Sci.* **2019**, *494*, 1119.
[59] L. Herbers, J. Minář, S. Stuckenberg, V. Küpers, D. Berghus, S. Nowak, M. Winter, P. Bieker, *Adv. Energy Sustainability Res.* **2023**, *4*, 2300153.
[60] P. Roering, G. M. Overhoff, K. L. Liu, M. Winter, G. Brunklaus, *ACS Appl. Mater. Interfaces* **2024**, *16*, 21932.
[61] H. Zhang, H. Wu, L. Wang, H. Xu, X. He, *J. Power Sources* **2021**, *492*, 229661.
[62] N. G. Connelly, W. E. Geiger, *Chem. Rev.* **1996**, *96*, 877.
[63] C. F. Marchiori, R. P. Carvalho, M. Ebadi, D. Brandell, C. M. Araujo, *Chem. Mater.* **2020**, *32*, 7237.
[64] F. Faglioni, B. V. Merinov, W. A. Goddard, B. Kozinsky, *Phys. Chem. Chem. Phys.* **2018**, *20*, 26098.
[65] L. Seidl, R. Grissa, L. Zhang, S. Trabesinger, C. Battaglia, *Adv. Mater. Interfaces* **2022**, *9*, 2100704.
[66] C.-P. S. Hsu, *Handbook of Instrumental Techniques for Analytical Chemistry*, Prentice Hall PTR, Upper Saddle River, NJ **1997**, p. 249.
[67] N. L. Alpert, W. E. Keiser, H. A. Szymanski, *IR: Theory and Practice of Infrared Spectroscopy*, Springer Science & Business Media, Berlin/New York **2012**.